

# Mode-Constrained Two-Stage Current Injection Optimization for Voltage Unbalance Mitigation in IBR-Rich Distribution Network

Tiantian Ji, *Student Member, IEEE*, Pengfeng Lin, *Member, IEEE*, Miao Zhu, *Member, IEEE*, Wentao Jiang, *Member, IEEE*, Xian Zhang, *Senior Member, IEEE*, Changyun Wen, *Fellow, IEEE*, Peng Wang, *Fellow, IEEE*

**Abstract**—Under unbalanced grid conditions, inverter-based resources (IBRs) are required to remain connected to the grid and provide reactive current injection to mitigate voltage unbalance at the point of common coupling. Most existing research focuses primarily on steady-state reference current generation under such conditions, whereas current overshoot and oscillations induced by reference-switching have been largely overlooked. Driven by this gap, this paper proposes a mode-constrained two-stage current injection optimization framework. In the first stage, the dominant oscillatory modes of a grid-connected IBR are identified through closed-loop transfer function modeling and eigenvalue analysis. In the second stage, a reference-switching trajectory optimization problem is formulated in the frequency domain, in which the trajectory is constructed through a virtual acceleration sequence. By maximizing the virtual energy contained in the sequence under spectral energy constraints, the fastest and optimal trajectory is indirectly obtained, and the excitation of dominant oscillatory modes during reference switching is thereby prevented. Since this framework is implemented at the reference level, it is fully compatible with existing controllers and adaptable to varying operating conditions. Simulation and experimental results confirm the effectiveness of the proposed optimization framework.

**Index Terms**—Inverter-based resources (IBRs), voltage unbalance mitigation (VUM), optimal trajectory design, frequency-domain optimization, current control.

## I. INTRODUCTION

### A. Research Background

With the accelerated transition of global energy structure towards renewable sources, inverter-based resources (IBRs) such as solar photovoltaic, wind power, and battery energy storage systems have been widely deployed in distribution networks [1], [2]. Unlike traditional power systems dominated by synchronous generators, the dynamics of these systems are mainly determined by the control schemes of their power electronic interfaces. Although large-scale integration of IBRs significantly

Manuscript received on 31 Aug, 2025; revised on 21 Nov, 2025; accepted on 17 Dec, 2025. This work is supported by Smart Grid-National Science and Technology Major Project 2025ZD0806600. (Corresponding author: Pengfeng Lin).

Pengfeng Lin, Tiantian Ji, and Miao Zhu are with Shanghai Jiao Tong University, China (Email: linpengfeng@ieee.org, {thekiterunner, miao.zhu}@sjtu.edu.cn).

Wentao Jiang is with Northwestern Polytechnical University, China (Email: ewtjiang@nwpu.edu.cn).

Xinan Zhang is with The University of Western Australia, Australia (Email: xinan.zhang@uwa.edu.au).

Changyun Wen is with Nanyang Tehchnological University, Singapore (Email: ecywen@ntu.edu.sg).

Peng Wang is with Nanjing Normal University, China (Email: epwang@ntu.edu.sg).

enhances grid flexibility and renewable energy hosting capabilities, their inherent low inertia leads to reduced system resilience to disturbances. Besides, the combination of nonlinear load and IBRs would induce serious power quality issues [1], [3], [4]. Among them, voltage unbalance (VU) has been widely recognized as one of the most critical problems, as it causes greater losses and heating effects, and may even trigger the disconnection of IBRs under severe unbalanced conditions [5]. Therefore, the development of advanced and effective voltage unbalance mitigation (VUM) methods in IBR-rich distribution networks is urgently needed.

### B. Literature Review

Traditionally, VUM in distribution networks relies on dedicated power electronic devices such as static var compensators (SVCs) and static synchronous compensators (STATCOMs) [6]–[8]. These devices regulate system voltage by flexibly injecting or absorbing reactive power at the point of common coupling (PCC). While effective, such solutions often entail high installation costs and limited deployment flexibility, especially in metropolitan areas where their electrical distribution rooms are densely occupied [9].

Recent literature has reported that increasing attentions are directed toward leveraging the existing IBR infrastructure for VUM, in both academia and industry. By re-purposing the residual capacity of IBRs beyond their primary power supply function, VUM can be achieved without additional hardware investments. Upon the adoption of IBRs, two major VUM control strategies have been established for distribution system applications, which are the virtual impedance (VI) approach [10]–[12] and the negative sequence current (NSC) injection approach [13]–[19]. The former one mitigates voltage unbalance by modifying the inverter’s output impedance. The latter, in contrast, actively injects negative sequence currents to compensate for asymmetrical voltage components. This sort of method provides a more direct and effective mitigation strategy without inducing any unnecessary voltage drops that could be observed in VI-based schemes. Early NSC-based approaches typically adopt rule-based control strategies [13]–[15], where the current references of IBRs under voltage unbalance conditions are derived from predefined proportional coefficients multiplied by the negative-sequence voltage component. While such methods offer simple implementations, they often fail to fully exploit the potential of IBRs for VUM [20]. To overcome these limitations, recent research has shifted toward optimization-based VUM

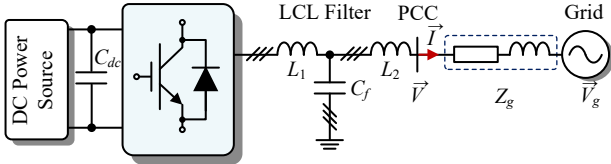


Fig. 1. Schematic diagram of a three-phase grid-connected IBR system.

strategies of IBRs [16]–[19], in which the positive- and negative-sequence current references are optimized as decision variables. For instance, an optimization model that takes into account grid impedance and current injection constraints is studied in [16], [17], and it helps to minimize the negative sequence voltage at PCC. However, due to the absence of essential constraints such as power balance between the AC and DC sides, the resulting current references may be infeasible in practical implementations. To tackle this issue, [18] incorporates active power/current constraints of IBRs into an optimization model and further provides analytical optima along with global optimality analyses. In [19], the load impedance at PCC is further incorporated into the optimization framework, thereby enhancing the applicability of the system model.

In spite of the efforts found in the above studies, however, it should be mentioned that they fall short of offering sufficient attention to the transient behaviors of IBRs in the midst of current reference changes. In fact, an abrupt variation in the current reference serves as a wide-spectrum excitation that could activate the inherent oscillatory modes of the system, particularly those with low damping ratios [21]. The excitation of such modes typically leads to current overshoot, oscillatory transients, and prolonged settling times. It may even result in instability issues if the system lacks sufficient damping or if the control parameters are poorly tuned. Furthermore, the dynamic interaction between the IBR and the external grid may reduce the effective damping of certain modes, making them more susceptible to being excited under reference changes or external disturbances [22], [23].

### C. Gap Identification and Contributions

In practical engineering, IBR control loops and their associated parameters are generally pre-defined by manufacturers and cannot be altered as per the needs of system operators. In addition, these controllers are typically tailored to specific operating points and control objectives. Variations in system conditions may shift the dominant oscillation frequency, thereby deteriorating the converter's dynamic performance. To ensure a smooth transition between two operating points, input shaping methods such as ramp-rate limiters and S-curve trajectories are extensively utilized to refine the reference-switching trajectory, thereby mitigating the transient excitation of underdamped modes at the source end [24]. Although these approaches are compatible with existing IBR controllers, they blindly filter out a large amount of high-frequency components in the reference signals, which unnecessarily prolongs the transition between two set points and compromises dynamic system performance. More advanced input trajectory shapers, such as the Zero Vibration Zero Derivative (ZZVD) shaper, can be designed to target certain oscillatory frequencies; however, because they operate as

digital filters on the reference signal, they inevitably introduce additional delays. When more oscillatory modes need to be handled, the total delay becomes even longer. In addition, these input shapers lack robustness and may fail when the system's modal frequencies drift. Apart from the above studies, several other trajectory planning methods, such as Model Predictive Control (MPC), have also been reported. However, these methods generally emphasize tracking a predetermined trajectory rather than generating one. For instance, in [25], an integrated MPC framework is developed to regulate the inductor current and multi-port output voltages of a single-input multiple-output boost converter. Although the inductor current reference can be adaptively adjusted based on the real-time load demand of each port, this reference is produced by an external supervisory module, rather than being synthesized within the MPC loop. Hence, the MPC still operates essentially as a tracking controller. Similarly, [26] proposes a continuous control-set MPC strategy for grid-connected converters, where zero steady-state error in sinusoidal current tracking is achieved by embedding resonant poles into an augmented state-space model. Overall, these MPC-based approaches focus on optimizing the control action to follow a pre-specified reference, whereas the generation of the reference trajectory itself is not addressed within the MPC formulation.

To achieve a faster possible dynamic response without exciting dominant underdamped oscillatory modes in a grid-connected IBR system, this paper proposes a mode-constrained two-stage current injection trajectory optimization framework. The first stage performs system modeling and eigenvalue analysis to identify the dominant oscillatory modes. Specifically, the system under study is a grid-connected IBR with dual sequence current control as shown in Fig. 2. Its dynamics are described by the closed-loop transfer function matrices formulated in positive- and negative-sequence  $dq$ -frame. In the second stage, a current reference trajectory (CRT) optimization problem is formulated to generate an optimal CRT (OCRT) that simultaneously ensures smooth and fast transitions and avoids oscillatory mode excitation. To this end, in this paper, the second-order difference of the CRT is interpreted as a “virtual acceleration”, analogous to physical acceleration in motion control systems. In physical systems, acceleration reflects the rate at which energy is delivered to a system. Therefore, the virtual energy can be introduced for the virtual acceleration sequence. On the one hand, maximizing the total virtual energy produces the fastest possible current-switching trajectory. On the other hand, frequency-domain energy constraints are imposed around the identified modal frequencies to suppress undesirable oscillations. Given that the CRT can be regarded as a double integral of the virtual acceleration, restricting the mode energy of the virtual acceleration sequence indirectly avoids the excitation of the oscillatory mode in the final current response. Compared with existing strategies, the proposed method offers the following advantages:

- 1) The introduction of virtual acceleration and virtual energy reformulates CRT optimization into a more systematic and tractable framework, which improves convergence and simplifies modeling.
- 2) A frequency-domain energy constraint is explicitly incorporated into the optimization framework. This formulation

- allows the flexible control of spectral energy and effectively avoids the excitation of dominant oscillatory modes.
- 3) The obtained OCRT is implemented at the reference level and requires no modification to existing control loops once the dominant oscillatory modes are identified.

The remainder of this article is organized as follows. Section II describes the system under study, along with its corresponding control strategy. Section III focuses on the first stage of the optimization process, identifying the dominant oscillatory modes through the system transfer function matrix. Section IV addresses the second stage, outlining the problem statement of the CRT optimization problem, including modeling and the selection of optimization parameters. Section V details the specific implementation of the two-stage optimization framework, supported by dynamic simulation and experimental results. Finally, Section VI summarizes this article and presents the main conclusions.

## II. SYSTEM DESCRIPTION

### A. System Configuration

Fig. 1 depicts the schematic diagram of a three-phase grid-connected IBR system. The DC power source, such as a PV panel or wind turbine, is interfaced with the AC grid through a voltage-source inverter followed by an LCL output filter.  $L_1$ ,  $L_2$ ,  $C_f$ , and  $Z_g$  denote the inverter-side inductor, the filter capacitor, the grid-side inductor of the LCL filter, respectively. Based on the Thévenin equivalent principle, the external AC grid could be modeled as a voltage source  $\vec{V}_g$  in series with a grid impedance  $Z_g = R_g + jX_g$ . Here,  $Z_g$  is the positive-sequence grid impedance, while its negative-sequence counterpart is typically approximated as the complex conjugate of  $Z_g$ .

The VU at the PCC primarily arises from the unbalanced grid. In a three-phase three-wire system, unbalanced electrical quantities can be decomposed into positive- and negative-sequence components. As revealed by (1), the IBR is capable of injecting controlled currents into the grid, thereby enabling active voltage regulation at the PCC and contributing to VUM.

$$\begin{cases} \vec{V}_p = \vec{V}_{gp} + (R_g + jX_g) \vec{I}_p \\ \vec{V}_n = \vec{V}_{gn} + (R_g - jX_g) \vec{I}_n \end{cases} \quad (1)$$

where  $\vec{V}$  and  $\vec{I}$  represent the PCC voltage and output currents, respectively. Subscripts “ $p$ ” and “ $n$ ” denote the positive- and negative-sequence components, respectively. This notation will be consistently adopted throughout the remainder of this article.

### B. Control Structure

A dual sequence current control is adopted to regulate the positive- and negative-sequence components of the output current as illustrated in Fig. 2. The sequence extraction (SE) of unbalanced electrical quantities is realized via a double second-order generalized integrator (DSOGI) module and a positive- and negative-sequence calculator (PNSC) module. The configurations and transfer functions of the two modules will be discussed in the subsequent section. A grid-current control structure with four filter inductor decoupling branches is applied.  $G_{del} = e^{-1.5T_s s}$  represents the control delay caused by sampling and computation, where  $T_s$  denotes the sampling

period. In our work, instead of integrating a phase lock loop, which easily induces instability, positive- and negative-sequence rotating reference frames with initial phases of zero are adopted, while no effects on steady state active/reactive power injection into the grid would occur [27], [28].

## III. STAGE ONE: THE IDENTIFICATION OF DOMINANT MODES

Identifying the system’s dominant underdamped oscillatory modes is the first step in implementing the two-stage CRT optimization framework. In this article, modal analysis is carried out in dual synchronous rotating reference frames. A major challenge arises from the dynamic coupling between positive- and negative-sequence currents, which complicates the accurate identification of system modes. This coupling is primarily due to the use of the SE, which narrows down the control bandwidth and introduces phase delays. Therefore, this section provides a detailed analysis of the coupling mechanism between the positive- and negative-sequence current channels. Subsequently, a closed-loop transfer function matrix is derived to quantitatively characterise the relationship between current references ( $i_{dp}^*$ ,  $i_{qp}^*$ ,  $i_{dn}^*$ , and  $i_{qn}^*$ ) and output currents ( $i_{dp}$ ,  $i_{qp}$ ,  $i_{dn}$ , and  $i_{qn}$ ). On this basis, the system’s dominant underdamped oscillatory modes are identified through Bode plots and pole-zero analysis.

### A. Coupling Mechanism Induced by SE

The detailed structure of SOGI is provided in the Fig. 3. It comprises two parallel paths: a band-pass filter  $H_D(s)$  and a quadrature signal generator  $H_Q(s)$ , whose transfer functions are defined as (2) and (3), respectively.

$$H_D(s) = \hat{i}_\alpha / i_\alpha = \hat{i}_\beta / i_\beta = \frac{k\omega_0 s}{s^2 + k\omega_0 s + \omega_0^2} \quad (2)$$

$$H_Q(s) = q\hat{i}_\alpha / i_\alpha = q\hat{i}_\beta / i_\beta = \frac{k\omega_0^2}{s^2 + k\omega_0 s + \omega_0^2} \quad (3)$$

where  $k$  determines the damping coefficient and  $\omega_0$  denotes the central frequency.

The PNSC module in Fig. 2 is described as

$$\begin{bmatrix} i'_{\alpha p} \\ i'_{\beta p} \end{bmatrix} = \frac{1}{2} \begin{bmatrix} 1 & -q \\ q & 1 \end{bmatrix} \begin{bmatrix} \hat{i}_\alpha \\ \hat{i}_\beta \end{bmatrix}, \quad \begin{bmatrix} i'_{\alpha n} \\ i'_{\beta n} \end{bmatrix} = \frac{1}{2} \begin{bmatrix} 1 & q \\ -q & 1 \end{bmatrix} \begin{bmatrix} \hat{i}_\alpha \\ \hat{i}_\beta \end{bmatrix}, \quad (4)$$

where  $q = e^{-j\pi/2}$ .

Combining (2), (3), and (4), the complex vector expressions of the positive- and negative-sequence components in the  $\alpha\beta$ -frame can be formulated as (5).

$$\begin{cases} i'_{\alpha\beta p} = i'_{\alpha p} + j i'_{\beta p} = 0.5(\hat{i}_\alpha - q\hat{i}_\beta) + j 0.5(q\hat{i}_\alpha + \hat{i}_\beta) \\ \quad = 0.5[H_D(s) + jH_Q(s)]i_{\alpha\beta}, \\ i'_{\alpha\beta n} = i'_{\alpha n} + j i'_{\beta n} = 0.5(\hat{i}_\alpha + q\hat{i}_\beta) - j 0.5(q\hat{i}_\alpha - \hat{i}_\beta) \\ \quad = 0.5[H_D(s) - jH_Q(s)]i_{\alpha\beta}. \end{cases} \quad (5)$$

Fundamentally, the Park transformation performs frequency spectrum shifting, namely,  $s_{dq+} = s_{\alpha\beta} + j\omega_0$ ,  $s_{dq-} = s_{\alpha\beta} - j\omega_0$ . The notation  $dq+$  denotes the positive-sequence synchronous rotating frame, whereas  $dq-$  denotes the negative-sequence

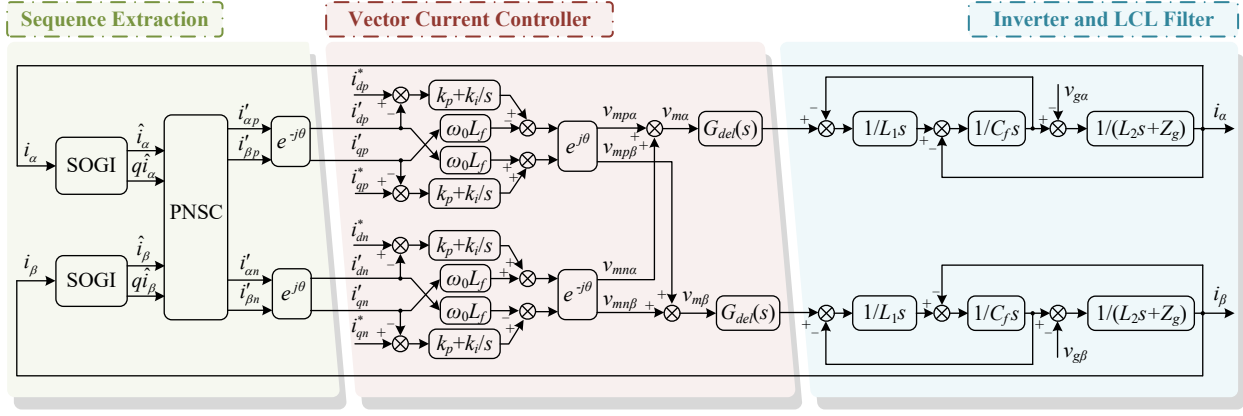


Fig. 2. Control block diagram of dual sequence current control with DSOGI.

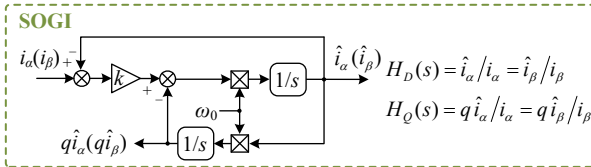


Fig. 3. Block Diagram of SOGI.

synchronous rotating frame. Accordingly, (5) can be rewritten as

$$\begin{cases} i'_{dqp} = 0.5 [H_D(s + j\omega_0) + jH_Q(s + j\omega_0)] i_{dq+}, \\ i'_{dqn} = 0.5 [H_D(s - j\omega_0) - jH_Q(s - j\omega_0)] i_{dq-}. \end{cases} \quad (6)$$

By separating the real and imaginary parts, the purely real-valued matrix form of (6) can be readily obtained, as shown in (7). The corresponding entries are given in (8).

$$\begin{cases} \begin{bmatrix} i'_{dp} \\ i'_{qp} \end{bmatrix} = \underbrace{\begin{bmatrix} H_{11p}(s) & H_{12p}(s) \\ H_{21p}(s) & H_{22p}(s) \end{bmatrix}}_{H_{DQp}(s)} \begin{bmatrix} i_{d+} \\ i_{q+} \end{bmatrix}, \\ \begin{bmatrix} i'_{dn} \\ i'_{qn} \end{bmatrix} = \underbrace{\begin{bmatrix} H_{11n}(s) & H_{12n}(s) \\ H_{21n}(s) & H_{22n}(s) \end{bmatrix}}_{H_{DQn}(s)} \begin{bmatrix} i_{d-} \\ i_{q-} \end{bmatrix}. \end{cases} \quad (7)$$

in which

$$\begin{cases} H_{11p}(s) = H_{22p}(s) = H_{11n}(s) = H_{22n}(s) \\ = \frac{k\omega_0 s^3 + k^2 \omega_0^2 s^2 + 4k\omega_0^3 s + 2k^2 \omega_0^4}{2s^4 + 4k\omega_0 s^3 + (2k^2 + 8)\omega_0^2 s^2 + 8k\omega_0^3 s + 2k^2 \omega_0^4} \\ H_{21p}(s) = -H_{12p}(s) = H_{12n}(s) = -H_{21n}(s) \\ = \frac{k^2 \omega_0^3 s}{2s^4 + 4k\omega_0 s^3 + (2k^2 + 8)\omega_0^2 s^2 + 8k\omega_0^3 s + 2k^2 \omega_0^4}. \end{cases} \quad (8)$$

For brevity, bold symbols are used for column vectors or matrices, such as  $\mathbf{i}_{dqp} = [i_{dp}; i_{qp}]$ , while complex variables like  $i_{dqp} = i_{dp} + ji_{qp}$  are not bolded. According to (7), when the three-phase currents  $\mathbf{i}_{abc}$  are unbalanced, directly mapping them into the positive-sequence rotating frame through the Park transformation yields  $\mathbf{i}_{dq+}$ , which contains a dc positive-sequence component  $i_{dqp}$  and a second-harmonic negative-sequence component  $i_{dqn,2\omega}$ .  $H_{DQp}(s)$  in (7) essentially acts as a filtering function that extracts the dc component  $i'_{dqp}$  for current control. The quantity  $i'_{dqp}$  can be interpreted as

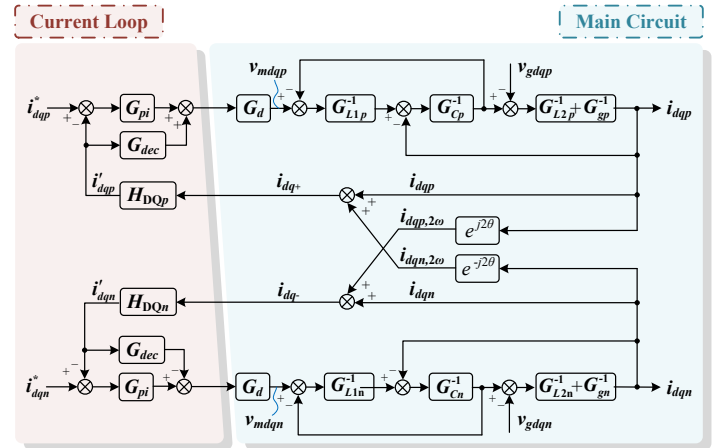


Fig. 4. Equivalent block diagram under dual synchronous reference frames.

the estimation of  $i_{dqp}$ , and under steady-state conditions, the estimated value  $i'_{dqp}$  coincides with the actual dc positive-sequence component  $i_{dqp}$ . Similarly,  $H_{DQpn}(s)$  serves as a filtering function in the negative-sequence rotating frame to extract the negative-sequence current for control.

Based on the above analysis, the equivalent control block diagram in Fig. 4 is obtained. The diagram includes the control loop and the main circuit, and both parts contain the corresponding positive- and negative-sequence networks. The operator  $e^{\pm j2\theta}$  in Fig. 4 represents the frequency shift between positive- and negative-sequence synchronous frames, i.e.,  $s_{dq+} = s_{dq-} + j2\omega_0$ ,  $s_{dq-} = s_{dq+} - j2\omega_0$ . It can be observed that the system exhibits cross-coupling between the two loops. Specifically, any variation in the positive-sequence current reference  $i_{dqp}^*$  induces a transient response in the negative-sequence channel due to cross-coupling, and vice versa. These transient components eventually decay to zero.

### B. System Modeling

In Fig. 4,  $G_{pi}$  and  $G_{dec}$  denote the PI controller and filter inductance decoupling paths, respectively, with explicit forms given in (9).  $G_d = G_{del} I$  represents the control delay matrix. The positive-sequence loop transfer function matrices of the plant are given in (10). The corresponding negative-sequence

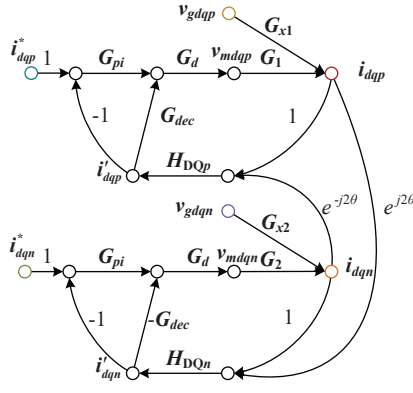


Fig. 5. Signal flow diagram of the studied system.

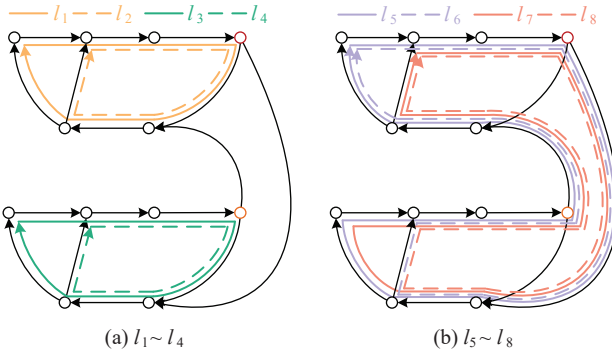


Fig. 6. Loop distribution within the signal flow diagram.

counterparts  $G_{L1n}$ ,  $G_{L2n}$ ,  $G_{Cn}$ , and  $G_{gn}$  can be obtained by substituting  $\omega_0$  with  $-\omega_0$  in (10).

$$G_{pi} = \left( k_p + \frac{k_i}{s} \right) I, \quad G_{dec} = \omega_0 L_f \begin{bmatrix} 0 & -1 \\ 1 & 0 \end{bmatrix}. \quad (9)$$

$$\begin{cases} G_{L1p} = L_1 P, & G_{Cp} = C_f P, \\ G_{L2p} = L_2 P, & G_{gp} = L_g P + R_g I. \end{cases} \quad (10)$$

where  $L_f = L_1 + L_2$ ,  $P = [s, -\omega_0; \omega_0, s]$ , and  $I$  denotes the identity matrix.

Based on Fig. 4, the expressions for the positive- and negative-sequence output currents in terms of the modulation voltage and grid voltage are derived as follows.

$$\begin{cases} i_{dqp} = \underbrace{[(I + G_{L1p} G_{Cp})(G_{L2p} + G_{gp}) + G_{L1p}]^{-1}}_{G_1} v_{mdqp} \\ \quad - \underbrace{[G_{L2p} + G_{gp} + G_{L1p} + G_{Cp}^{-1}]^{-1}}_{G_{x1}} v_{gdqp}, \\ i_{dqn} = \underbrace{[(I + G_{L1n} G_{Cn})(G_{L2n} + G_{gn}) + G_{L1n}]^{-1}}_{G_2} v_{mdqn} \\ \quad - \underbrace{[G_{L2n} + G_{gn} + G_{L1n} + G_{Cn}^{-1}]^{-1}}_{G_{x2}} v_{gdqn}. \end{cases} \quad (11)$$

Building on this, the equivalent control diagram in Fig. 4 is further transformed into the signal flow diagram in Fig. 5. As shown in Fig. 6, the diagram contains eight internal feedback loops, whose individual loop gains are given in Table I. Fur-

TABLE I  
LOOP GAINS IN THE SIGNAL FLOW DIAGRAM

Parameters	Value
$l_1(s)$	$-G_1 G_d G_{pi} H_{DQp}$
$l_2(s)$	$G_1 G_d G_{dec} H_{DQp}$
$l_3(s)$	$-G_2 G_d G_{pi} H_{DQn}$
$l_4(s)$	$-G_2 G_d G_{dec} H_{DQn}$
$l_5(s)$	$(G_2 G_d G_{pi} H_{DQn}) _{s=s+j2\omega_0} G_1 G_d G_{pi} H_{DQp}$
$l_6(s)$	$(G_2 G_d G_{dec} H_{DQn}) _{s=s+j2\omega_0} G_1 G_d G_{pi} H_{DQp}$
$l_7(s)$	$-(G_2 G_d G_{pi} H_{DQn}) _{s=s+j2\omega_0} G_1 G_d G_{dec} H_{DQp},$
$l_8(s)$	$-(G_2 G_d G_{dec} H_{DQn}) _{s=s+j2\omega_0} G_1 G_d G_{dec} H_{DQp}$

thermore, according to Mason's gain formula, the corresponding signal flow graph determinant equals

$$\Delta = I + G_4 - G_5|_{s=s+j2\omega_0} G_4 + G_4 G_5. \quad (12)$$

in which

$$\begin{aligned} G_4 &= G_1 G_d (G_{pi} - G_{dec}) H_{DQp}, \\ G_5 &= G_2 G_d (G_{pi} + G_{dec}) H_{DQp}. \end{aligned} \quad (13)$$

Furthermore, the forward path functions  $p_j$  between the source and sink nodes of each transfer function, along with their corresponding signal flow graph cofactors  $\Delta_j$ , are calculated as follows.

1) From  $i_{dqp}^*$  to  $i_{dqp}$ :

$$T_p = \frac{p_1 \Delta_1}{\Delta}, \quad p_1 = G_1 G_d G_{pi}, \quad \Delta_1 = I - G_5. \quad (14)$$

2) From  $i_{dqn}^*$  to  $i_{dqn}$ :

$$T_n = \frac{p_2 \Delta_2}{\Delta}, \quad p_2 = G_2 G_d G_{pi}, \quad \Delta_2 = I + G_4. \quad (15)$$

3) From  $i_{dqp}^*$  to  $i_{dqn}$ :

$$T_{p2n} = \frac{p_3 \Delta_3}{\Delta}, \quad p_3 = -(G_1 G_d G_{pi})|_{s=s+j2\omega_0} G_5, \quad \Delta_3 = I. \quad (16)$$

4) From  $i_{dqn}^*$  to  $i_{dqp}$ :

$$T_{n2p} = \frac{p_4 \Delta_4}{\Delta}, \quad p_4 = -(G_2 G_d G_{pi})|_{s=s-j2\omega_0} G_4, \quad \Delta_4 = I. \quad (17)$$

The above transfer function matrices are complex-valued. By separating the real and imaginary parts, their real-valued representations can be derived. In addition, since frequency shifting is applied to the forward paths  $p_3$  and  $p_4$  in steps 3) and 4), the input signals  $i_{dqp}^*$  and  $i_{dqn}^*$  must also undergo the same frequency shift to ensure consistency. The overall transfer function matrices are expressed as:

$$\begin{bmatrix} i_{dqp}(s) \\ i_{dqn}(s) \end{bmatrix} = \begin{bmatrix} T_p(s) & 0_{2 \times 2} \\ 0_{2 \times 2} & T_n(s) \end{bmatrix} \begin{bmatrix} i_{dqp}^*(s) \\ i_{dqn}^*(s) \end{bmatrix} + \begin{bmatrix} 0_{2 \times 2} & T_{n2p}(s) \\ T_{p2n}(s) & 0_{2 \times 2} \end{bmatrix} \begin{bmatrix} i_{dqp}^*(s - j2\omega_0) \\ i_{dqn}^*(s + j2\omega_0) \end{bmatrix}. \quad (18)$$

By analyzing the Bode diagrams of the transfer functions defined in (18), the dominant underdamped modes that govern the system dynamics can be identified.

#### IV. STAGE TWO: CURRENT REFERENCE TRAJECTORY OPTIMIZATION FORMULATION

With the dominant oscillatory modes identified earlier, this section is devoted to designing an OCRT that avoids exciting these modes.

### A. Analysis of Input Signals and System Response in Frequency Domain

According to Fourier transform theory, any real-valued signal  $x(t)$  can be expressed as a superposition of an infinite number of sinusoidal components, each with a specific frequency  $\omega$ , amplitude  $V(\omega)$ , and phase  $\phi(\omega)$ , as shown in (19)

$$x(t) = \int_0^{+\infty} V(\omega) \cos[\omega t + \phi(\omega)] d\omega. \quad (19)$$

An approximately linear system, when viewed in the frequency domain, behaves as a filter whose frequency response determines the amplification or attenuation of different frequency components of input signals. In particular, the dominant poles of the system dictate its modal behavior. When the dominant poles are underdamped, the system tends to exhibit oscillatory responses during transients, especially when the input contains spectral components near those modal frequencies. Consequently, if the input signal does not contain spectral components around the system's dominant modal frequencies, the system response will not exhibit oscillations at the corresponding frequencies.

### B. Problem Formulation

Based on the above analysis, it is desirable to generate a CRT with minimal spectral energy around the system's dominant modal frequencies. Considering the finite sampling rate of practical digital control systems, the CRT is formulated as a discrete-time sequence. However, directly optimizing this trajectory amounts to adjusting individual sampling points independently, without a unifying structure or guiding principle. Then, the resultant trajectory is often neither smooth nor reliably convergent. To address this issue, the current sequence is modeled as a discrete signal that allows second-order difference, from which the notions of "virtual velocity", defined as the first-order difference of the current sequence and "virtual acceleration", defined as the second-order difference of the current sequence, are introduced. By imposing spectral constraints on the virtual acceleration around dominant modal frequencies, the corresponding spectral components in the CRT can be effectively suppressed to avoid undesired mode excitation.

1) *DFT of the Virtual Acceleration Sequence:* Let  $\mathbf{a} = [a_0, a_1, \dots, a_{L-1}]^T \in \mathbb{R}^L$  denote the acceleration sequence of length  $L$ . The DFT matrix  $\mathbf{W} \in \mathbb{C}^{L \times L}$  is defined by

$$\mathbf{W}(n, k) = \frac{1}{L} e^{-j \frac{2\pi n k}{L}}, \quad n, k = 0, 1, \dots, L-1. \quad (20)$$

The DFT coefficient vector can then be obtained as (21) and the  $n$ -th coefficient is given explicitly by (22). The frequency resolution is  $\Delta f = f_s/L$ . Zero-padding technique can optionally be applied by extending the acceleration sequence to a longer length  $L_{\text{pad}}$ , which preserves the true spectral content while improving the frequency resolution [24].

$$\mathbf{A} = \mathbf{W}\mathbf{a} \in \mathbb{C}^L. \quad (21)$$

$$A_n = \frac{1}{L} \sum_{k=0}^{L-1} a_k e^{-j \frac{2\pi n k}{L}}, \quad n = 0, 1, \dots, L-1, \quad (22)$$

2) *Spectral Energy Constraint:* Let the set of modes of interest be

$$F = \{f^{(1)}, f^{(2)}, \dots, f^{(M)}\}, \quad (23)$$

where  $f^{(m)}$  denotes the frequency of the  $m$ -th dominant mode, and  $M$  denotes the number of dominant modes.

Due to damping-induced spectral broadening and the coarse frequency resolution of DFT, the spectral energy of each mode spreads over multiple frequency points rather than being confined to a single point. To account for this, for the  $m$ -th mode, the corresponding frequency band is defined by

$$B^{(m)} = [f^{(m)} - \delta f_{tol}, f^{(m)} + \delta f_{tol}], \quad (24)$$

where  $\delta f_{tol}$  specifies the frequency tolerance, and its value will be explained in the next subsection.

For each  $B^{(m)}$ , the index set of DFT points is given in (25) and its total spectral energy is constrained as (26).

$$N^{(m)} = \{n \mid f_n \in B^{(m)}\}, \quad m = 1, \dots, M. \quad (25)$$

$$\sum_{n \in N^{(m)}} |A_n|^2 \leq \rho \max_{0 \leq n < L} |A_n|^2, \quad m = 1, \dots, M. \quad (26)$$

Here, the left-hand side of (26) represents the total energy within the  $m$ -th frequency band, while the right-hand side corresponds to the global maximum energy among all frequency points in the sequence.  $\rho \in (0, 1)$  is a tunable suppression ratio, where a smaller  $\rho$  indicates that the energy in the band should occupy a smaller fraction of the global maximum energy.

Furthermore, we denote a binary selection matrix  $\mathbf{S}^{(m)} \in \mathbb{R}^{L \times L}$  with its entries satisfy  $\mathbf{S}^{(m)}(n, n) = 1$  if  $n \in N^{(m)}$  and 0 otherwise. For each mode of interest, there is a corresponding selection matrix. The operation  $\mathbf{S}^{(m)}\mathbf{A}$  yields the DFT coefficients corresponding to the  $m$ -th frequency band. For example, if  $N^{(1)} = \{7, 8, 9\}$ , then  $\mathbf{S}^{(1)}\mathbf{A} = [0, \dots, 0, A_7, A_8, A_9, 0, \dots, 0]^T$ .

Note that the inequality constraint in (26) is non-convex. To address this issue, an auxiliary variable  $t \geq 0$  is introduced as

$$|A_n|^2 \leq t, \quad n = 0, \dots, L-1. \quad (27)$$

By variable substitution, (26) can be further rewritten as

$$\|\mathbf{S}^{(m)}\mathbf{A}\|_2^2 \leq \rho t, \quad m = 1, \dots, M. \quad (28)$$

3) *Boundary Constraints:* To ensure that the optimized reference trajectory converges smoothly to its terminal point without leaving residual oscillations, explicit boundary constraints should be enforced.

First, the terminal virtual velocity of the current sequence should vanish, i.e.,  $v_L = 0$ . Assuming the initial velocity and current are zero (i.e.,  $v_0 = 0, i_0 = 0$ ), this constraint can be equivalently expressed as (29) using the forward Euler method.

$$v_L = T_s \sum_{k=0}^{L-1} a_k = 0. \quad (29)$$

Second, the CRT is normalized to unity, resulting in a standardized general trajectory. Owing to the linearity of DFT, the resulting trajectory can be scaled to any desired amplitude without altering its spectral characteristics. Hence, the last element is determined as

$$i_{L+1} = T_s^2 \sum_{k=0}^{L-1} (L-k) a_k = 1. \quad (30)$$

**4) Objective:** Let us recall a basic principle from the motion control field: achieving the fastest transition between two positions with zero terminal velocity is a classical time-optimal control problem. The optimal motion trajectory is characterized by utilizing the maximum allowable acceleration, such that the system acquires the maximum possible energy from external actuation during the acceleration phase, which is then dissipated during the deceleration phase. In this sense, acquiring maximum energy is equivalent to applying the largest admissible acceleration within the actuation limits. Inheriting this principle, the proposed formulation defines the virtual energy  $E(\mathbf{a})$  of the acceleration sequence as the squared  $\ell_2$ -norm, which quantifies the overall acceleration energy subject to actuation limits.

$$E(\mathbf{a}) = \|\mathbf{a}\|_2^2 = \mathbf{a}^T \mathbf{a}. \quad (31)$$

In summary, the CRT optimization problem can be formulated as a second-order cone programming (SOCP), which allows it to be directly handled by commercial solvers.

$$\begin{aligned} & \underset{\mathbf{a}}{\text{maximize}} \quad E(\mathbf{a}) \\ & \text{subject to} \quad (28) - (30). \end{aligned} \quad (32)$$

By solving (32), the optimal virtual acceleration sequence  $\mathbf{a}^*$  can be obtained, and performing a double integration on this sequence yields the OCRT  $\mathbf{i}^*$ . Beyond the optimization horizon,  $\mathbf{i}^*$  is held constant at its terminal value to provide a consistent input for the remaining time.

### C. Optimization Parameter Selection Guideline

Frequency tolerance  $\delta f_{tol}$  and optimization horizon  $L$  are not fixed parameters but can be determined based on the dominant modes and the system's sampling frequency  $f_s$ .

**1)  $\delta f_{tol}$  selection:** For the  $m$ -th dominant mode with complex-conjugate poles  $p^{(m)} = -\sigma^{(m)} \pm j\omega_d^{(m)}$ , its undamped natural frequency (rad/s) and damping ratio are, respectively,

$$\omega_n^{(m)} = \sqrt{(\sigma^{(m)})^2 + (\omega_d^{(m)})^2}, \quad \zeta^{(m)} = \sigma^{(m)} / \omega_n^{(m)}. \quad (33)$$

When the damping ratio is small, its half-power bandwidth (in Hz) can be approximated as

$$\Delta f_{hp}^{(m)} \approx 2\zeta^{(m)}\omega_n^{(m)} / 2\pi. \quad (34)$$

The modal frequencies may shift due to parameter uncertainties or variations in grid impedance. To prevent the CRT from becoming invalid under such drift, a safety factor  $\alpha$  (typically 1.0–1.5) is introduced in (35). By slightly widening the allowable frequency intervals, the safety factor provides sufficient margin to accommodate these potential deviations.

$$\delta f_{tol}^{(m)} = \alpha \Delta f_{hp}^{(m)} / 2 = \alpha \sigma^{(m)} / 2\pi. \quad (35)$$

To reduce complexity, the multiple tolerances  $\{\delta f_{tol}^{(m)}\}_{m=1}^M$  are replaced by their maximum value.

$$\delta f_{tol} = \max\{\delta f_{tol}^{(1)}, \delta f_{tol}^{(2)}, \dots, \delta f_{tol}^{(M)}\}. \quad (36)$$

**2)  $L$  selection:**  $L$  cannot be obtained in closed form, but it can be determined through a top-down traversal search. The upper bound of  $L$  is first established: when the frequency resolution  $\Delta f$  equals the tolerance  $\delta f_{tol}$ , each mode band contains at least

two DFT points, which is sufficient to ensure reliable optimization. Increasing  $L$  further would only enlarge the problem size without significantly improving performance. Therefore,  $f_s/\delta f_{tol}$  is selected as the upper limit for  $L$ . Subsequently,  $L$  can be gradually reduced from this upper bound, e.g., in steps of 50, until the smallest  $L$  that still ensures satisfactory performance is obtained.

**3)  $L_{pad}$  selection:** Zero-padding may optionally be applied to the sequence when performing the DFT of the virtual acceleration sequence. The padded length  $L_{pad}$  is typically selected as a power of two, which enables the use of FFT algorithms and thus improves computational efficiency.

### D. Implementation Details

The complete two-stage optimization framework is illustrated in Fig. 7. In the present work, the optimization process is performed offline to obtain the normalized OCRT. During real-time operation, the local inverter controller generates actual reference trajectories online by scaling the normalized OCRT according to the desired operating point. However, it is necessary to point out that the proposed framework is open to revision for online implementation. In such a revision, a host computer is responsible for solving or updating the frequency-domain optimization problem, while a slave device (DSP-based inverter controller) scales and executes OCRTs in real time. Moreover, since the optimization problem has been formulated as an SOCP, numerous mature schemes can be readily incorporated to speed up the solution process and enhance its online feasibility, such as warm-start strategies [29], parallelized interior point algorithms [30], and alternating direction methods of multipliers tailored for SOCP [31]. With the support of a high-performance host computer and efficient algorithms, the computational burden can be significantly reduced, which makes online optimization practically achievable.

From a hierarchical control perspective, the proposed framework is fully compatible with the communication architectures in modern distribution networks. Specifically, the energy management system (EMS) operates at the dispatch level and issues steady-state current commands at relatively slow intervals (from seconds to minutes). After receiving these commands from EMS, the local controller generates actual reference trajectories through amplitude scaling. This entire calculation process is entirely performed within the local control layer, which operates at a high sampling frequency (e.g., 10kHz). It should also be emphasized that the proposed framework introduces no extra communication burden to the system.

## V. IMPLEMENTATION AND VALIDATION

To validate the efficiency of this framework, simulations and experiments are conducted under two unbalanced grid test cases (Case-1, Case-2). The system parameters employed in both simulations and experiments are identical, as summarized in Table II. Fig. 8 illustrates the experimental hardware platform, which corresponds to the grid-connected IBR system shown in Fig. 1. The DC bus voltage is set by an IT6000D Series programmable DC power supply. The switch signals of the inverter are generated from DSpace 1202. A Tektronix MSO44 Series oscilloscope records the experimental waveforms. We

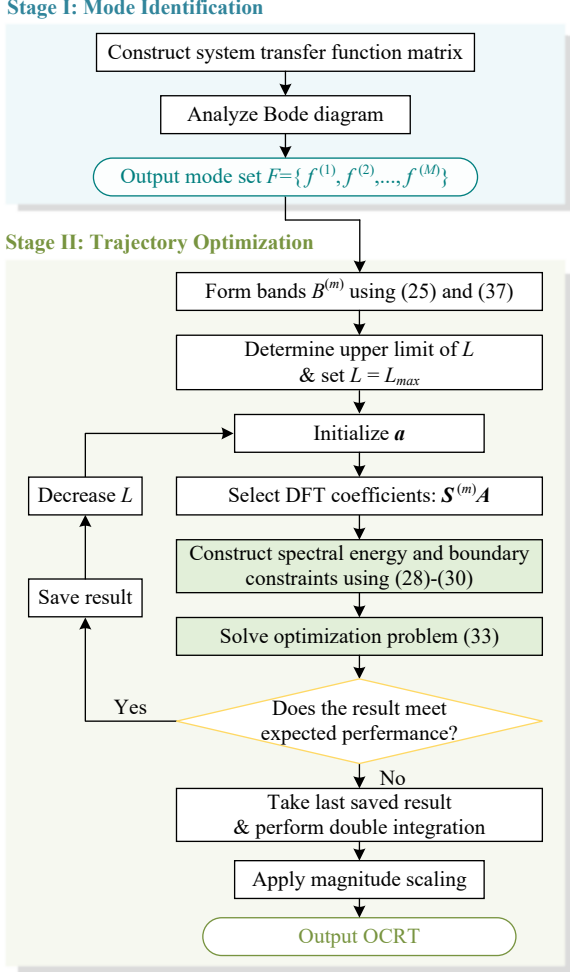


Fig. 7. Complete flowchart of the proposed two-stage optimization framework.

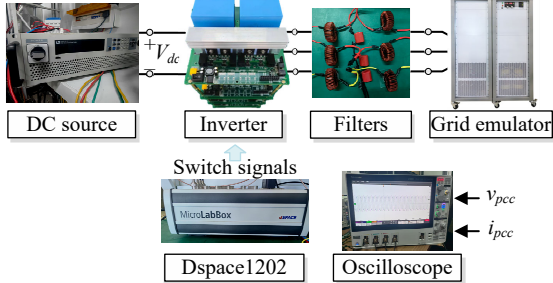


Fig. 8. Experimental platform.

adopt the NSC injection strategy described in [32] to compute the steady-state current references. This strategy ensures optimal VUM at the PCC when the IBR output current amplitude is constrained. Table III summarizes the grid-voltage settings and the corresponding current injection references of the two cases. Case-1 represents a mild VU condition, and Case-2 is a moderate one.

#### A. Model Verification and Mode Identification

Case-1 is simulated to verify the model's correctness and to extract the system's dominant modes. Before activating the NSC injection strategy, only the positive-sequence  $d$ -axis current  $I_{dp} = 10A$  is injected, while the other current components are set to zero. At  $t = 0.5s$ , the NSC injection strategy is enabled. The simulated step responses are compared with the theoretical

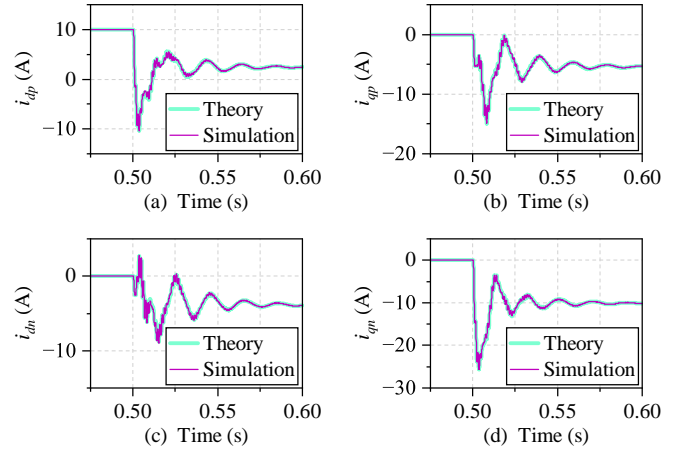


Fig. 9. Comparisons between theoretical results and simulation waveforms.

step responses derived from the transfer function matrices, as shown in Fig. 9. The close agreement between these responses validates the accuracy of the model. By inspecting Fig. 4, it can be observed that the system is identical in the two synchronous rotating reference frames, except for the opposite rotation directions. Accordingly, the positive- and negative-sequence transfer function matrices are identical, i.e.,  $T_p = T_n$  and the cross-coupling terms also satisfy  $T_{p2n} = T_{n2p}$ . Moreover, each of these transfer function matrices exhibits internal symmetry: the diagonal entries are identical, and the off-diagonal entries are negatives of each other. Therefore, only the Bode diagrams of  $T_p(1, 1)$ ,  $T_p(1, 2)$ ,  $T_{p2n}(1, 1)$ , and  $T_{p2n}(1, 2)$  are drawn in Fig. 10. As can be observed, the three resonance peaks correspond to the three modes of interest in this work. Their dominant pole pairs are  $-42.6 \pm j314.2$ ,  $-41.9 \pm j5192.4$ , and  $-41.9 \pm j4564.1$ , respectively.

TABLE II  
SYSTEM SPECIFICATIONS

Description	Symbol	Value
DC-link voltage	$V_{dc}$	400V
AC voltage amplitude	$V_g$	155.5V
Nominal power	$P_0$	4kW
Maximum current limit	$I_{lim}$	15A
Nominal frequency	$f_0$	50Hz
Converter-side inductor of LCL filter	$L_1$	1.75mH
Capacitor of LCL filter	$C_f$	20μF
Grid-side inductor of LCL filter	$L_2$	3.5mH
Grid resistance	$R_g$	1.1Ω
Grid inductance	$L_g$	3.5mH
Damping coefficient of SOGI	$k$	0.707
Current loop proportional gain	$k_p$	10
Current loop integral gain	$k_i$	400
Sampling frequency	$f_s$	10kHz

TABLE III  
CASE SETTINGS AND CURRENT INJECTION VALUES

Case	Grid Voltage (V)	Current Reference Value (A)
Case-1	$V_{gp} = 140.0 \angle 0^\circ$ $V_{gn} = 15.6 \angle -45^\circ$	$I_{dp} = 2.44, I_{qp} = -5.49$ $I_{dn} = -3.95, I_{qn} = -10.14$
Case-2	$V_{gp} = 155.5 \angle 0^\circ$ $V_{gn} = 46.7 \angle -45^\circ$	$I_{dp} = 0, I_{qp} = 0$ $I_{dn} = -4.74, I_{qn} = -14.23$

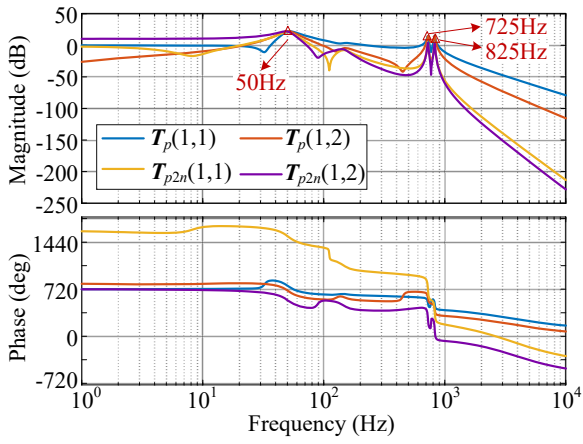


Fig. 10. Bode diagrams of  $T_p(1,1)$ ,  $T_p(1,2)$ ,  $T_{p2n}(1,1)$ , and  $T_{p2n}(1,2)$ .

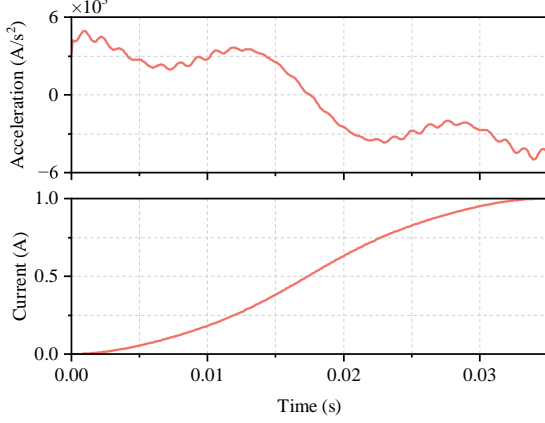


Fig. 11. Optimal acceleration sequence along with the corresponding OCRT.

### B. Trajectory Optimization and Simulation Comparisons

The proposed CRT optimization procedure in Stage II is then performed, with the corresponding optimization parameters summarized in Table IV. Fig. 11 presents the derived optimal acceleration sequence along with the corresponding OCRT.

To enable a deeper comparison, the ZZVD input shaper for each mode is designed according to [24], denoted by  $\mathcal{H}_m$  ( $m = 1, 2, 3$ ). The detailed impulse times and amplitudes of the three shapers are summarized in TABLE V. By cascading the three shapers, i.e., performing convolution operations among them as  $\mathcal{H}(t) = \mathcal{H}_1(t) * \mathcal{H}_2(t) * \mathcal{H}_3(t)$ , a composite shaper is derived that simultaneously suppresses the oscillations of all three modes. The actual input signal  $u(t)$  is then obtained by convolving the step signal  $r(t)$  with the composite shaper, i.e.,  $u(t) = r(t) * \mathcal{H}(t)$ . Three types of reference-switching trajectories are employed in this work: the step, the step shaped by  $\mathcal{H}(t)$ , and the OCRT. For clarity, the corresponding system responses are referred to as the step response, the shaped response, and the OCRT response, respectively.

TABLE IV  
OPTIMIZATION PARAMETERS

Description	Symbol	Value
Optimization horizon	$L$	350
Padded sequence length	$L_{pad}$	1024
Safety factor	$\alpha$	1.5
Frequency tolerance	$\delta f_{tol}$	10Hz
Spectral suppression ratio	$\rho$	0.0002

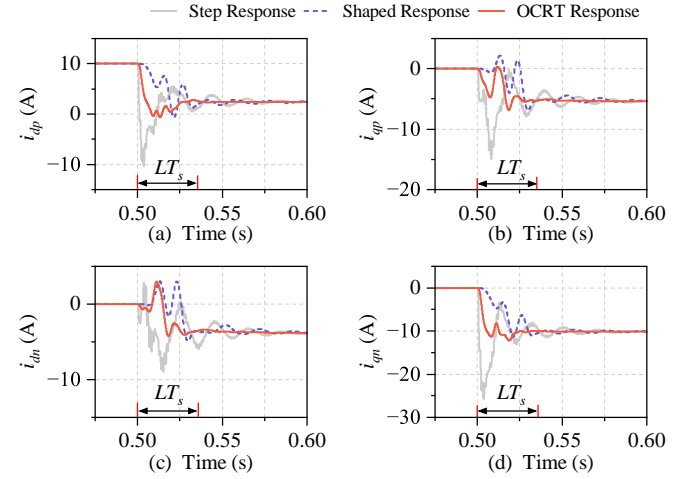


Fig. 12. Transient response comparisons under three types of reference-switching trajectories.

Fig. 12 compares the three types of system transient responses in Case-1.  $LT_s$  represents the duration of the OCRT, i.e.,  $350 \times 10^{-4} = 0.035$ s. Initially,  $I_{dp}$  is set to 10A, while all other current references are zero. At  $t = 0.5$ s, the NSC injection strategy is enabled, and current references are switched to the values listed in Table III following the three different trajectories. It can be observed that the transient performance of the system is significantly improved when the proposed OCRT is applied. After 0.035s, it nearly reaches steady state with only minimal residual oscillations, whereas the step and shaped responses still exhibit varying degrees of oscillations. The 0.5–0.6s segments of the three response curves in Fig. 12(a) are further analyzed using FFT, and their spectral magnitudes are visualized in Fig. 13. Only three frequency bands of interest are shown, with magnitudes expressed as percentages relative to the DC component. When the OCRT is employed, the oscillatory components are substantially reduced. Taking the mode at 50Hz as an example, the spectral magnitude decreases by approximately 93.6% compared with the step response and by 65.2% compared with the shaped response.

### C. Experiment Validation

Experiments are conducted under the two representative cases summarized in Table III. At the beginning of each experiment, only  $I_{dp} = 10$ A is injected, while all other current references remain zero. The NSC injection strategy is enabled at  $t = 0.5$ s and disabled at  $t = 0.7$ s. Fig. 14 and Fig. 15 present the shaped responses and the OCRT responses under Case-1, respectively. By comparing Fig. 14(b) and Fig. 15(b), it can be observed that both reference-switching trajectories suppress the oscillations during the transient process to different extents; however, the proposed OCRT method exhibits superior transient performance with smaller current overshoots and smoother current transitions. Specifically, during the NSC injection and stopping

TABLE V  
PARAMETERS OF ZZVD INPUT SHAPER

Shaper	Impulse time	Impulse amplitude
$\mathcal{H}_1$	[0,0.0101,0.0202,0.0303]	[0.2210,0.4336,0.2835,0.0618]
$\mathcal{H}_2$	[0,6.8968e-04,0.0014,0.0021]	[0.12978,0.3797,0.3702,0.1203]
$\mathcal{H}_3$	[0,6.0608e-04,0.0012,0.0018]	[0.1298,0.3797,0.3702,0.1203]

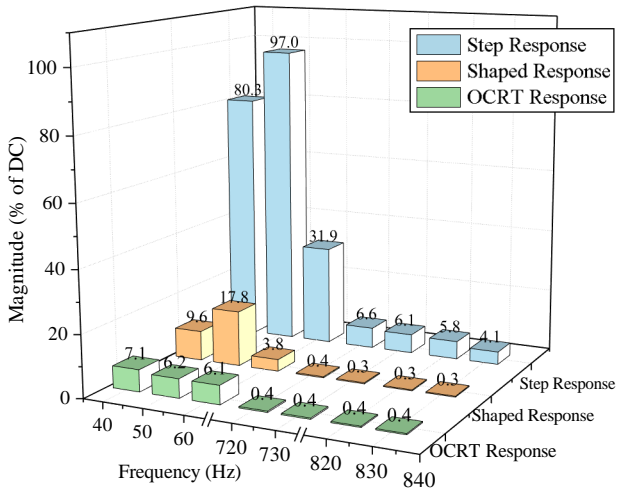


Fig. 13. Spectral magnitude comparisons of  $i_{dp}$  responses under three types of reference-switching trajectories.

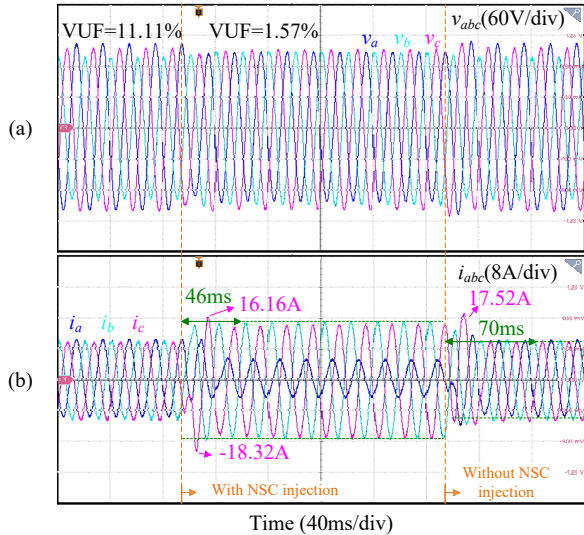


Fig. 14. Shaped responses of PCC voltage and output current under Case-1.

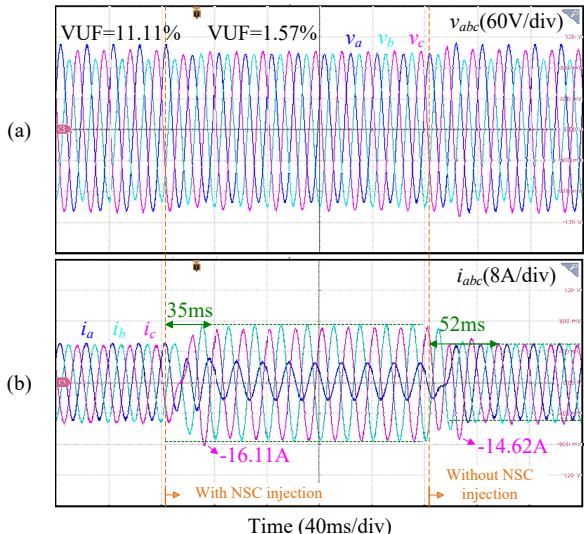


Fig. 15. OCRT responses of PCC voltage and output current under Case-1.

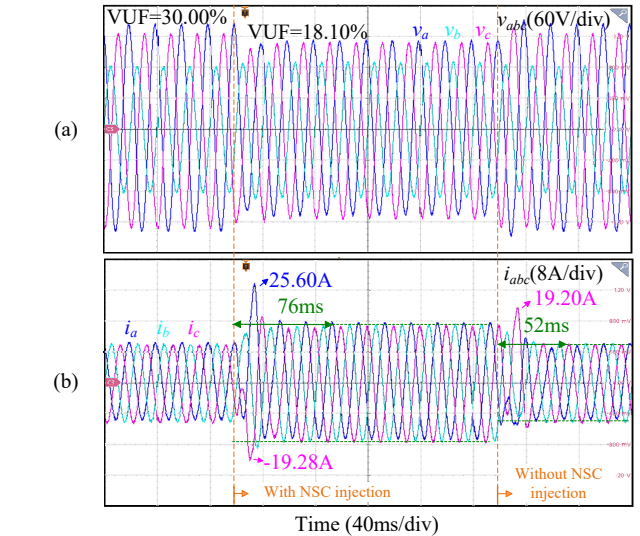


Fig. 16. Shaped responses of PCC voltage and output current under Case-2.

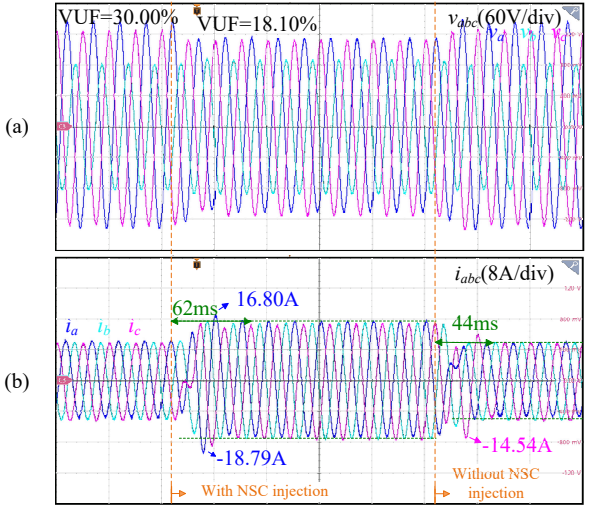


Fig. 17. OCRT responses of PCC voltage and output current under Case-2.

processes, the phase-C peak currents respectively reach -18.32A and 17.52A when the ZVDD shaper is applied. In contrast, they are reduced to -16.11A and -14.62A with the proposed OCRT method, corresponding to a 12.1% and 16.5% reduction in peak magnitude, respectively. Moreover, with the ZZVD shaper, the system settling times are 46ms and 70ms, whereas the proposed OCRT reduces them to 35ms and 52ms, respectively. The steady-state voltage unbalance factor (VUF) decreases from 11.11% to 1.57% in both experiments once the NSC injection strategy is activated.

Fig. 16 and Fig. 17 present the shaped responses and the OCRT responses under Case-2, respectively. A similar observation can be made by comparing Fig. 16(b) and Fig. 17(b). Specifically, during the NSC injection process, the phase-A peak current reaches 25.60A with the ZVDD shaper, whereas it is reduced to -18.79A with the proposed OCRT method. Likewise, after exiting the NSC injection strategy, the phase-C peak current reaches 19.20A with the ZVDD shaper, while it is lowered to -14.54A with the OCRT method. Consistently, with the ZZVD shaper, the system settling times are 76ms and 52ms, whereas the proposed OCRT reduces them to 62ms and 44ms, respectively. The steady-state VUF decreases from 30.00% to

TABLE VI  
COMPARATIVE ANALYSIS OF DIFFERENT TRAJECTORY PLANNING METHODS

Method	Control Objective	Mode-Constraint Flexibility	Time Duration of Trajectory	Computational Complexity	Robustness
MPC [25], [26], [33], [34]	Achieve zero tracking error	No	/	High	High
Input Shaper [35], [36]	Suppress oscillations during reference transitions	No	Long (increases with the number of modes)	Low	Moderate
S-curve Trajectory [24], [37]	Suppress oscillations during reference transitions	No	Fixed (determined by the predefined transition time)	Low	Low
Proposed OCRT	Fast reference transitions without oscillations	Yes	Minimal	Moderate	High

18.10% in both experiments once the NSC injection strategy is activated.

Both simulation and experimental results indicate that the proposed OCRT significantly enhances transient performance without compromising steady-state VUM. In addition, it can be seamlessly integrated with the steady-state current reference optimization method.

## VI. DISCUSSION

### A. Robustness Analysis

Component parameters exhibit manufacturing tolerances during mass production, and grid impedance may vary under different field conditions. These factors may lead to shifts in the system's modal frequencies. To enhance robustness, a safety factor has already been incorporated in the selection of the constrained frequency bands, so that the designed OCRT inherently tolerates moderate modal frequency drift. If stronger robustness is desired, the distributions of relevant parameters (e.g., component values and grid impedance) can be modeled as normal or other reasonable distributions [38]. Monte-Carlo simulations are then performed, where each sampled set of parameters undergoes the same modal frequency extraction process in Stage I. This procedure yields the distributions of the system's modal frequencies, from which their mean values and confidence intervals are obtained. These confidence intervals are subsequently adopted as the constrained frequency bands in Stage II. In this manner, the optimized OCRT remains robust against parameter and impedance variations. This entire process can be completed offline at the factory, without the need for on-site commissioning.

### B. Extension to Multi-IBR System

The proposed two-stage framework can also be extended to a multi-IBR system with necessary modifications in its Stage I modeling process. As the number of IBRs increases, the dimensionality of the transfer-function matrix grows rapidly [39]; therefore, the transfer-function modeling in Stage I should be replaced by an impedance-based modeling [40], [41] or other suitable alternatives [42], [43]. Take the impedance-based modeling as an example, each IBR is equivalently modeled as a current source in parallel with its output admittance, which implicitly includes its internal control characteristics. The grid is modeled as an ideal voltage source in series with a grid impedance. IBRs and grid impedance are connected at the PCC, and the network impedance matrix can then be formulated accordingly. The dominant mode can be found by calculating

the smallest eigenvalue of the network admittance matrix [40], [41]. Once the dominant modes of the system are identified, the OCRT can be obtained using the frequency-domain optimization algorithm described in Section IV. Moreover, for multi-input multi-output systems, all input signals share the same mode set. Therefore, identical mode constraints can be simultaneously imposed on all inverter reference trajectories to achieve coordinated damping and dynamic consistency. In essence, all procedures are consistently developed within the unified “mode identification–trajectory optimization” framework.

To the best of our knowledge, few existing studies have explored the concept of accelerating system stabilization by precisely avoiding the external excitation of underdamped modes, nor have they incorporated the modal spectral energy as an explicit constraint within the optimization formulation. Therefore, it follows that the proposed two-stage optimization framework is a fundamental work to provide a new perspective for dynamic trajectory planning in converter-dominated systems. To highlight its superiority, Table VI summarizes the comparative characteristics and advantages of the proposed method.

## VII. CONCLUSION

This paper proposed a two-stage trajectory optimization framework for the current reference design. Key findings are summarized as follows:

- 1) By modeling the CRT as a second-order sequence, the optimization target is expressed in terms of the virtual-acceleration sequence, which greatly simplifies the optimization process.
- 2) DFT analysis and spectral energy constraints are innovatively incorporated into the optimization model. Moreover, the optimization procedure and parameter selection are explicitly clarified.
- 3) Simulation and experimental results confirm that the proposed optimization framework effectively improves transient performance during reference-switching processes.
- 4) The proposed framework offers a non-intrusive solution for avoiding the excitation of oscillatory modes. This design philosophy is particularly suited to scenarios where the inverter controller is closed-source, and hardware modification is not allowed.

## REFERENCES

- [1] S. Mallapaty *et al.*, “How china could be carbon neutral by mid-century,” *Nature*, vol. 586, no. 7830, pp. 482–483, 2020.
- [2] P. Lin, L. Du, H. Zhang, M. Zhu, J. Ma, and P. Wang, “Power lever: To transform interlinking architecture in hybrid ac/dc microgrids community,” *IEEE Transactions on Industrial Electronics*, 2025.

- [3] P. Lin, Q. Meng, M. Zhu, A. M. Y. M. Ghias, and F. Blaabjerg, "Dynamic circuit-based unified power regulation for hybrid ac/dc/ds microgrids: A comprehensive approach to static and transient control," *IEEE Transactions on Industrial Electronics*, pp. 1–12, 2025.
- [4] J. Wu, F. Guo, F. Yang, C. Wen, M.-Y. Chow, and F. Boem, "Resilient net zero: An overview on secure control methods for networked microgrids," *IEEE Industrial Electronics Magazine*, pp. 2–14, 2025.
- [5] A. von Jouanne and B. Banerjee, "Assessment of voltage unbalance," *IEEE Transactions on Power Delivery*, vol. 16, no. 4, pp. 782–790, 2001.
- [6] L. Wang, C.-S. Lam, and M.-C. Wong, "Hybrid structure of static var compensator and hybrid active power filter (svc/hapf) for medium-voltage heavy loads compensation," *IEEE Transactions on Industrial Electronics*, vol. 65, no. 6, pp. 4432–4442, 2018.
- [7] A. Camacho, M. Castilla, J. Miret, M. Velasco, and R. Guzman, "Positive-sequence voltage control, full negative-sequence cancellation, and current limitation for static compensators," *IEEE Journal of Emerging and Selected Topics in Power Electronics*, vol. 9, no. 6, pp. 6613–6623, 2021.
- [8] L. Wang, C.-S. Lam, and M.-C. Wong, "Multifunctional hybrid structure of svc and capacitive grid-connected inverter (svc/cgi) for active power injection and nonactive power compensation," *IEEE Transactions on Industrial Electronics*, vol. 66, no. 3, pp. 1660–1670, 2019.
- [9] A. Mousaei, M. Gheisarnejad, and M. Khooban, "Challenges and opportunities of facts devices interacting with electric vehicles in distribution networks: A technological review," *Journal of Energy Storage*, vol. 73, p. 108860, 2023. [Online]. Available: <https://www.sciencedirect.com/science/article/pii/S2352152X23022570>
- [10] A. S. Vijay, N. Parth, S. Doolla, and M. C. Chandorkar, "An adaptive virtual impedance control for improving power sharing among inverters in islanded ac microgrids," *IEEE Transactions on Smart Grid*, vol. 12, no. 4, pp. 2991–3003, 2021.
- [11] M. E. Akdogan, D. Ramasubramanian, and S. Ahmed, "Control and stability analysis of grid-connected inverters in an unbalanced and distorted weak grid using mdsogi based selective virtual impedance," *IEEE Transactions on Industry Applications*, vol. 61, no. 2, pp. 2182–2192, 2025.
- [12] Y. Wang, J. Tang, J. Si, X. Xiao, P. Zhou, and J. Zhao, "Power quality enhancement in islanded microgrids via closed-loop adaptive virtual impedance control," *Protection and Control of Modern Power Systems*, vol. 8, no. 1, pp. 1–17, 2023.
- [13] T. Neumann, T. Wijnhoven, G. Deconinck, and I. Erlich, "Enhanced dynamic voltage control of type 4 wind turbines during unbalanced grid faults," *IEEE Transactions on Energy Conversion*, vol. 30, no. 4, pp. 1650–1659, 2015.
- [14] V. A. Almeida, G. N. Taranto, and J. M. T. Marinho, "Phasor-domain dynamic model of asymmetric current injection controller for converter-interfaced generator," *Journal of Modern Power Systems and Clean Energy*, vol. 9, no. 6, pp. 1269–1278, 2021.
- [15] N. R. Merritt, C. Chakraborty, and P. Bajpai, "New voltage control strategies for vsc-based dg units in an unbalanced microgrid," *IEEE Transactions on Sustainable Energy*, vol. 8, no. 3, pp. 1127–1139, 2017.
- [16] A. Camacho, M. Castilla, J. Miret, P. Martí, and M. Velasco, "Maximizing positive sequence voltage support in inductive-resistive grids for distributed generation inverters during voltage sags," in *IECON 2016 - 42nd Annual Conference of the IEEE Industrial Electronics Society*, 2016, pp. 2343–2348.
- [17] A. Camacho, M. Castilla, J. Miret, L. G. de Vicuña, and R. Guzman, "Positive and negative sequence control strategies to maximize the voltage support in resistive-inductive grids during grid faults," *IEEE Transactions on Power Electronics*, vol. 33, no. 6, pp. 5362–5373, 2018.
- [18] Y. Guo, B. C. Pal, and R. A. Jabr, "On the optimality of voltage unbalance attenuation by inverters," *IEEE Transactions on Sustainable Energy*, vol. 13, no. 3, pp. 1492–1506, 2022.
- [19] B. R., P. Bajpai, C. Chakraborty, M. Malakondaiah, and B. K. Kumar, "Adaptive dynamic voltage support scheme for fault ride-through operation of a microgrid," *IEEE Transactions on Sustainable Energy*, vol. 14, no. 2, pp. 974–986, 2023.
- [20] Ö. Göksu, R. Teodorescu, C. L. Bak, F. Iov, and P. C. Kjær, "Instability of wind turbine converters during current injection to low voltage grid faults and pll frequency based stability solution," *IEEE Transactions on Power Systems*, vol. 29, no. 4, pp. 1683–1691, 2014.
- [21] R. Dorf and R. Bishop, *Modern Control Systems*. Pearson Prentice Hall, 2008. [Online]. Available: <https://books.google.com/books?id=V-FpzJP5bEIC>
- [22] M. Zhang, Y. Zhang, and Q. Xu, "Transfer learning based online impedance identification for modular multilevel converters," *IEEE Transactions on Power Electronics*, vol. 38, no. 10, pp. 12 207–12 218, 2023.
- [23] X. Niu, Y. Qu, P. Lin, C. Cui, M. Sahani, C. Zhang, and S. K. Panda, "A tight grid-forming control framework for grid-connected inverters under large grid frequency drops with wide range of scr and x/r," *IEEE Transactions on Power Electronics*, pp. 1–13, 2025.
- [24] L. Biagiotti and C. Melchiorri, *Trajectory planning for automatic machines and robots*. Springer Science & Business Media, 2008.
- [25] V. Sukanya, G. V. Sumesh, and B. Bijukumar, "An integrated mpc strategy for minimizing cross-regulation in simo boost converters based on voltage and inductor current control," *IEEE Transactions on Industrial Electronics*, vol. 72, no. 10, pp. 10 684–10 695, 2025.
- [26] Y. Arias-Esquivel, R. Cardenas-Dobson, M. Uriarte, M. Diaz, and L. Tarisciotti, "An advanced zero-error continuous control set model predictive controller for low voltage ride through of grid-connected power converters," *IEEE Transactions on Industrial Electronics*, pp. 1–12, 2025.
- [27] Q.-C. Zhong, P.-L. Nguyen, Z. Ma, and W. Sheng, "Self-synchronized synchronverters: Inverters without a dedicated synchronization unit," *IEEE Transactions on Power Electronics*, vol. 29, no. 2, pp. 617–630, 2014.
- [28] J. Ma, W. Song, S. Jiao, J. Zhao, and X. Feng, "Power calculation for direct power control of single-phase three-level rectifiers without phase-locked loop," *IEEE Transactions on Industrial Electronics*, vol. 63, no. 5, pp. 2871–2882, 2016.
- [29] A. Bambade, F. Schramm, S. El-Kazdadi, S. Caron, A. Taylor, and J. Carpenter, "Proxqp: an efficient and versatile quadratic programming solver for real-time robotics applications and beyond," *IEEE Transactions on Robotics*, pp. 1–19, 2025.
- [30] M. D'Apuzzo and M. Marino, "Parallel computational issues of an interior point method for solving large bound-constrained quadratic programming problems," *Parallel Computing*, vol. 29, no. 4, pp. 467–483, 2003, parallel computing in numerical optimization. [Online]. Available: <https://www.sciencedirect.com/science/article/pii/S0167819103000176>
- [31] T.-H. Chang, M. Hong, W.-C. Liao, and X. Wang, "Asynchronous distributed admm for large-scale optimization—part i: Algorithm and convergence analysis," *IEEE Transactions on Signal Processing*, vol. 64, no. 12, pp. 3118–3130, 2016.
- [32] T. Ji, P. Lin, C. Zhang, M. Zhu, and S. Wen, "Collaborative current injection optimization strategy of multiple inverter-based sources under unbalanced grid," in *2025 IEEE Industry Applications Society Annual Meeting (IAS)*, 2025, pp. 1–5.
- [33] R. O. Ramírez, J. R. Espinoza, F. Villarroel, E. Maurelia, and M. E. Reyes, "A novel hybrid finite control set model predictive control scheme with reduced switching," *IEEE Transactions on Industrial Electronics*, vol. 61, no. 11, pp. 5912–5920, 2014.
- [34] B. Araya, C. Garcia, P. Acuna, R. Aguilera, C. Castillo, D. Sanchez, and J. Rodriguez, "Virtual vector optimal switching sequence model predictive control for computational burden reduction," in *2024 IEEE 9th Southern Power Electronics Conference (SPEC)*, 2024, pp. 1–6.
- [35] W. Singhose, "Command shaping for flexible systems: A review of the first 50 years," *International journal of precision engineering and manufacturing*, vol. 10, no. 4, pp. 153–168, 2009.
- [36] C.-G. Kang, R. Hassan, and K.-Y. Kim, "Analysis of a generalized zvd shaper using impulse vectors," *International Journal of Control, Automation and Systems*, vol. 18, no. 8, pp. 2088–2094, 2020.
- [37] W. Jun, W. Kai, and D. WuXue, "Slider movement planning based on improved s-curve acceleration algorithms for servo presses," *Materials Research Proceedings*, vol. 44.
- [38] C. Song and R. Kawai, "Monte carlo and variance reduction methods for structural reliability analysis: A comprehensive review," *Probabilistic Engineering Mechanics*, vol. 73, p. 103479, 2023. [Online]. Available: <https://www.sciencedirect.com/science/article/pii/S0266892023000681>
- [39] Y. Gu, N. Bottrell, and T. C. Green, "Reduced-order models for representing converters in power system studies," *IEEE Transactions on Power Electronics*, vol. 33, no. 4, pp. 3644–3654, 2018.
- [40] W. Xu, Z. Huang, Y. Cui, and H. Wang, "Harmonic resonance mode analysis," *IEEE Transactions on Power Delivery*, vol. 20, no. 2, pp. 1182–1190, 2005.
- [41] S. Varricchio, S. Gomes, and N. Martins, "Modal analysis of industrial system harmonics using the s-domain approach," *IEEE Transactions on Power Delivery*, vol. 19, no. 3, pp. 1232–1237, 2004.
- [42] B. Nouri, L. Kocewiak, S. Shah, P. Koralewicz, V. Gevorgian, and P. Sorensen, "Generic multi-frequency modelling of converter-connected renewable energy generators considering frequency and sequence couplings," *IEEE Transactions on Energy Conversion*, vol. 37, no. 1, pp. 547–559, 2022.
- [43] X. Wang and F. Blaabjerg, "Harmonic stability in power electronic-based power systems: Concept, modeling, and analysis," *IEEE Transactions on Smart Grid*, vol. 10, no. 3, pp. 2858–2870, 2019.

**Tiantian Ji** (Student Member, IEEE) received the B.Sc. degree in electrical engineering from Tianjin University, Tianjin, China, in 2024. She is currently working toward the M.Sc. degree in electrical engineering at the Shanghai Jiao Tong University, Shanghai, China. Her research interests include renewable energy generation and power electronic energized power system.

**Peng Wang** (Fellow, IEEE) was born in Shanxi, China, 1955. He received the B.Sc. degree from Xian Jiaotong University, Xi'an, China, in 1978, the M.Sc. degree from the Taiyuan University of Technology, Taiyuan, China, in 1987, and the M.Sc. and Ph.D. degrees from the University of Saskatchewan, Saskatoon, SK, Canada, in 1995 and 1998, respectively. He is currently a Professor with the School of Electrical and Electronic Engineering, Nanyang Technology University, Nanyang, Singapore. He is now with Nanjing Normal University.

**Pengfeng Lin** (Member, IEEE) received the B.S. and M.S. degree in electrical engineering from Southwest Jiao Tong University, China, in 2013 and 2015 respectively, and the Ph.D. degree in Interdisciplinary Graduate Programme from Nanyang Technological University, Singapore, in 2020. He was with Energy Research Institute @ NTU as a Research Fellow and with Électricité de France (EDF) as a Smart Grid Energy Expert / Research Scientist. He is in the global top 2% of Scientists released by Standard University. He is currently an Assistant Professor at Shanghai Jiao Tong University. His research interests include power system stability / reliability analyses, smart grid cyber-physical security, and artificial intelligence analytics.

**Miao Zhu** (Senior Member, IEEE) received the B.Sc. degree from Southeast University, China, in 2001 and the Ph.D. degree from Nanyang Technological University, Singapore in 2009, both in electrical engineering. From 2008 to 2009, he was with Meiden Asia Pte Ltd, Singapore, as an R&D Engineer. After that, he had been a Scientist in the Experimental Power Grid Centre (EPGC), A\*STAR, Singapore. In Aug. 2012, he joined Shanghai Jiao Tong University (SJTU), China. Currently, he is the Distinguished Professor in the School of Electrical Engineering, SJTU and the Vice Director of State Energy Smart Grid (Shanghai) R&D Centre. Since 2018, he has been the Vice Chairman of both IEEE PELS Shanghai Chapter and IEEE IES Shanghai Chapter. He has also been the Chair man of IEEE IAS Shanghai Chapter since 2019. Prof. Zhu is the recipient of 2009 IEEE Power Electronics Society Prize Letter Award. In 2010, he was awarded the World Future Foundation PhD Prize in Environmental and Sustainability Research. In 2018, he has been appointed as the Chief Scientist of National Key R&D Program of China (2018YFB0904100). His research interests include power converters, renewable energy generation, DC distributed network and DC grid.

**Wentao Jiang** (Member, IEEE) received the B.Eng. degree from Xi'an University of Technology, Xi'an, China, in 2011, the M.Sc. degree from the National University of Singapore, Singapore, in 2013, and the Ph.D. degree from Nanyang Technological University, Singapore, in 2018, all in electrical engineering. He was working in Energy Research Institute @ NTU (ERI@N), Singapore, as a Research Fellow, from 2018 to 2020. He is currently an Associate Professor with the College of Automation, Northwestern Polytechnical University, Xi'an, China. His current research focuses on modeling and control of the converters, dc microgrid, and multilelectric-aircraft (MEA) power systems.

**Xinan Zhang** (Senior Member, IEEE) received the B.E. degree in electrical engineering and automation from Fudan University, Shanghai, China, in 2008. He received the Ph.D. degree from Nanyang Technological University (NTU), Singapore, in 2014. He joined the University of Western Australia as a Senior Lecturer in 2019, where he is currently an Associate Professor. His research interests include electrical machine drives, control and modulation of power electronic converters, and design of hybrid energy storage systems.

**Changyun Wen** (Fellow, IEEE) received the B.Eng. degree in automation from Xi'an Jiaotong University, Xi'an, China, in 1983, and the Ph.D. degree in electrical engineering from the University of Newcastle, Callaghan, NSW, Australia, in 1990. From August 1989 to August 1991, he was a Post-Doctoral Fellow with the University of Adelaide, Adelaide, SA, Australia. Since August 1991, he has been with Nanyang Technological University, Singapore, where he is currently a Full Professor. His main research activities are in the areas of control systems and applications, cyber physical systems, smart grids, and complex systems and networks.